Tailoring High-Entropy Oxides as Emerging Radiative Materials for Daytime Passive Cooling

Borghesi, Costanza; Fabiani, Claudia; Bondi, Roberto; Latterini, Loredana; Castelli, Ivano E.; Pisello, Anna Laura; Giorgi, Giacomo

Published in:
Chemistry of Materials

Link to article, DOI:
10.1021/acs.chemmater.3c01205

Publication date:
2023

Document Version
Publisher's PDF, also known as Version of record

CHEMISTRY OF MATERIALS

pubs.acs.org/cm
Article

Tailoring High-Entropy Oxides as Emerging Radiative Materials for Daytime Passive Cooling

Costanza Borghesi, Claudia Fabiani, Roberto Bondi, Loredana Latterini, Ivano E. Castelli,* Anna Laura Pisello,* and Giacomo Giorgi*

Cite This: *Chem. Mater.* 2023, 35, 10384−10393
Read Online

ABSTRACT: In the framework of intense research about high-entropy materials and their applications in energy-oriented technologies, in the present work, we discuss the potential applicability of selected oxides and of the alloys they form at different concentrations for daytime radiative cooling implementation. In particular, by combining density functional theory and the finite difference method, we provide an unbiased, scattering-free description of structural, electronic, and dynamic features of the best candidates, showing the required strong radiative properties for passive cooling while offering the benefits of affordability and compatibility with commercial coating fabrication processes.

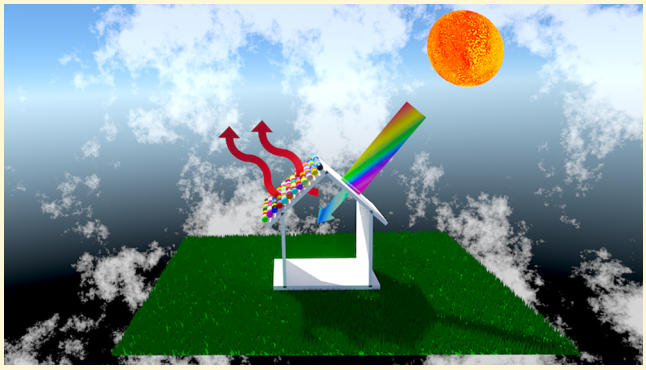

■ INTRODUCTION

The rise of the CO_2 concentration in the atmosphere represents an extremely severe and harmful issue intertwined with the global temperature increase. This concentration is rising primarily because of fossil fuel consumption for energy production. Heating, ventilation, and air conditioning systems (HVAC) play a primary role in this uncomfortable scenario, highly impacting the anthropogenic CO_2 emissions, exploiting electricity mainly produced from nonrenewable fossil fuels, and, in many cases, responsible for local heat dissipation as well. Most air conditioning (AC) systems still work with those technologies that release waste heat into the environment with subsequent outdoor local temperature increases.[1] Some of these outdated technologies still use hydrofluorocarbons, despite their largely demonstrated hazardousness.[2] The tight connection between the climate crisis and artificial heating/cooling is thus clear and threatens to become more severe as the global population grows. In particular, urban contexts, where currently 68% of the global population lives, are characterized by local overheating—typically referred to as Urban Heat Islands (UHIs)—with even more impact, as documented in more than 300 cities around the globe.[3−7] Hence, the investigation of renewable energy sources has been (and still is) a topic of deep interest, as demonstrated by the many pieces of research focusing on solar energy conversion processes, a consequence of recently discovered high performing materials (see, among the others, refs 8−12). However, as the energy−environment nexus is getting more and more evident, the time has come to combine energy production from renewables with strategies to mitigate detrimental urban overheating effects.[13]

In this direction, an extremely powerful approach has been proposed in the past decade to capitalize on a physical phenomenon, i.e., passive radiative cooling,[14−21] by which an object is able to dissipate heat at specific frequencies. Passive radiative cooling is a natural nocturnal phenomenon (in a highly thermally emissive regime) that can cool surfaces without energy consumption. Passive coolers directly emit heat through a transparent spectral window of the atmosphere (the so-called "atmospheric sky window", 8−13 μm) into the cold universe, which, with a temperature of 3 K, functions as an infinite heat sink. Therefore, when applied over buildings' envelopes, they have been demonstrated to reach subambient surface temperature, improving indoor−outdoor comfort and saving energy in the built environment.

Because of its impressive potential and inherent low costs, such a technique attracts deep interest from the paint production and building construction industries. It has been shown indeed that radiative cooling also occurs during the day[16,22,23] and can be used to cool a surface below ambient temperature even under direct sunlight if the thermal emission of the surface through the sky window exceeds its absorption

Received: May 17, 2023
Revised: October 3, 2023
Accepted: October 3, 2023
Published: October 23, 2023

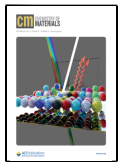

https://doi.org/10.1021/acs.chemmater.3c01205
Chem. Mater. 2023, 35, 10384−10393

of sunlight. Nevertheless, the transition from nocturnal to diurnal conditions drastically changes the scenario, and exploiting radiative cooling turns out to be a challenging task. Accordingly, devices able to induce passive daytime radiative cooling (PDRC) are under intense investigation. These devices are formed by a reflective layer (usually a metallic element) and a radiative cooling layer[17,20] where the latter is in charge of minimizing the absorption in the visible (VIS) region and of emitting in specific wavebands in the mid-infrared (IR).[16,22,24] The performance of the cooler deteriorates as fractions of the incident solar light are absorbed. Thus, the first *mandatory* feature is a material that minimizes the solar absorption: absorbing 10% of the solar radiation would indeed correspond to a rise of T from ∼200 K to room T, frustrating the final goal of such a setup.[16] The intrinsic difficulty in finding a single material able to properly deal with the IR and VIS region has motivated the usage of metamaterials and expensive (nano)photonic structures.[16,17,22] Initial attempts to find a single material with interesting properties have focused on $CaCO_3$[25] and other Mg-based compounds[26] and on porous materials.[27]

The evident lack of atomistic knowledge of the structural and optoelectronic features of the materials constituting the radiative cooling layer is boosting research in this direction. Only very recently have a few papers focused on the metrics (i.e., a suitable bandgap larger than the upper bound of energy in the solar spectrum, 4.13 eV, and a high number of IR-active optical resonance phonon modes in the sky window) accessible from first-principles calculations. These contributions compared the performance of SiO_2 (the standard material for PDRC) and $BaSO_4$ (a suggested alternative), paving the way toward the usage of ab initio atomistic simulations for innovative material development.[28]

Our aim is here to theoretically predict novel materials by exploiting the concepts behind the formation of high-entropy materials[29,30] and specifically of high-entropy oxides (HEOs).[31] The concept that encompasses the existence of such materials is that, by increasing the number of ionic components,[32] the entropic factor (ΔS_{mix}) becomes dominant in the Gibbs free energy equation. As a consequence of their broad structural diversity, this class of materials has been recently shown to have a huge potential in several device-oriented applications, among others, in dielectric uses,[33] in ion batteries,[34,35] in photo-[36] and electrocatalysis,[37,38] in energy storage,[39] and in low thermal conductivity.[40] Therefore, in order to perform our analysis, we initially start with the fluorite polymorph of $Y_2Ce_2O_7$,[41] an oxide composed of Y_2O_3[42] and CeO_2, which has been recently reported to have very appealing features as a material for PDRC—both free-standing and Fe-doped—embodying the characteristics of a good solar reflector and of an efficient IR emitter.[43] Keeping in mind the suggested metrics for an ideal radiator (vide supra),[28] we apply them to such precursor compounds that we in parallel have synthesized and initially characterized, to the intermediates (still synthesized and partly characterized), and to the final HEO $(Y_{0.25}Sc_{0.25}Ga_{0.25}In_{0.25})_2Si_2O_7$ (hereafter also $(YSGI)_2Si_2O_7$) resulting from our theoretical screening study. Our analysis reveals that $(YSGI)_2Si_2O_7$ has superior features as a material for PDRC: it indeed embodies the features of a wide bandgap and (almost) infinite dispersion material (frustrating any residual possible excitation) and those of an excellent IR emitter (smoothly and evenly spreading IR-active modes in the atmospheric sky window).

Thus, combining experimental and theoretical efforts, our present analysis aims to pave the way to the search for environmentally friendly and sustainable materials for passive daytime radiative cooling that can possibly gain wide commercial application with a particular focus on the built environment, with the final aim of mitigating urban heat islands. Importantly, to the best of our knowledge, our work discloses for the first time a new application, as materials for PDRC, for high-entropy oxides, further broadening the range of applications of this class of materials that promise to be the philosopher's stone of materials science in the years to come.

■ METHODS

First-principles calculations were performed by means of the Vienna Ab-initio Simulation Package (VASP)[44−47] using the electron exchange−correlation functional of Perdew−Burke−Ernzerhof (PBE)[48] for structural optimization. A cutoff energy of 520 eV is used in the projector augmented wave (PAW) method.[49,50] A 2 × 2 × 2 and a 3 × 2 × 5 k-point mesh was exploited for sampling the Brillouin zone (BZ) of the cubic and of the monoclinic system, respectively. Phonons were computed using the PHONOPY package with the finite displacement method,[51] employing a 2 × 1 × 2 supercell for the monoclinic compounds to capture the dynamics of the oxides accurately (88 atoms). For the phonon calculation, 2 × 2 × 2 (cubic) and 2 × 3 × 3 (monoclinic) k-point meshes were applied to the systems. All atoms of the supercell have been fully optimized (ions and lattice parameters) until forces were lower than 0.005 eV/Å. To improve over the PBE calculated ones, the electronic properties have been calculated by means of the Heyd−Scuseria−Ernzerhof (HSE06) hybrid functional.[52] The quasi-particle (QP) energies for $(YSGI)_2Si_2O_7$ are calculated within the "one-shot" G_0W_0 framework, adding 1078 empty states above the valence band maximum (VBM), which correspond to ∼140 eV, and sampling the BZ with 16 k-points. The number of frequency points is set to 120. The plane-wave cutoff is the default one (400 eV), while the cutoff for response function is set to 267 eV. The optical excitation energies and spectra are obtained solving the Bethe−Salpeter equation (BSE) in order to include excitonic and local-field effects.[53] The Tamm−Damcoff approximation is here considered,[53,54] while 20 (20) occupied (unoccupied) states are used to build up the excitonic matrix.

In order to obtain random solid solutions with controlled compositions on each sublattice and to build all structural input files of the generated Special Quasirandom Structures (SQS)[55] for the considered alloys we exploited the mcsqs[56] Monte Carlo SQS code of the Alloy Theoretic Automated Toolkit (ATAT).[57−59] The mcsqs algorithm exploits the cluster expansion theory to find the minimally sized supercell approximation whose cluster correlation functions as the best possible match to those of the targeted random structure. Using the output of the VASP data, we have processed the resultant ComputedEntry (extrated from Materials Project API)[60] using the MaterialsProjectCompatibility class of pymatgen's compatibility module to apply adjustments to the energies of the oxide anions to calculate the convex hull and eventually generate the phase diagram.

■ RESULTS AND DISCUSSION

Building up the appropriate atomic structure is the first step toward reliable prediction of the thermodynamic, kinetic, electronic, and phonon properties of HEOs. Accordingly, moving from available experimental data[43] we initially calculated the structural parameters of fluorite $Y_2Ce_2O_7$ polymorph (space group *Fm*3*m*, 227), obtaining results (a = 10.88 Å, @PAW/PBE) in agreement with previous[61,62] and with our experimental XRD data (see Figure 1). The optimized fluorite $Y_2Ce_2O_7$ structure is reported in Figure 2a. The HSE06 (PAW/PBE) calculated bandgap (direct at Γ) is 3.28 eV (1.54 eV) perfectly matching the experimental gap (3.29 eV).[43]

https://doi.org/10.1021/acs.chemmater.3c01205
Chem. Mater. 2023, 35, 10384−10393

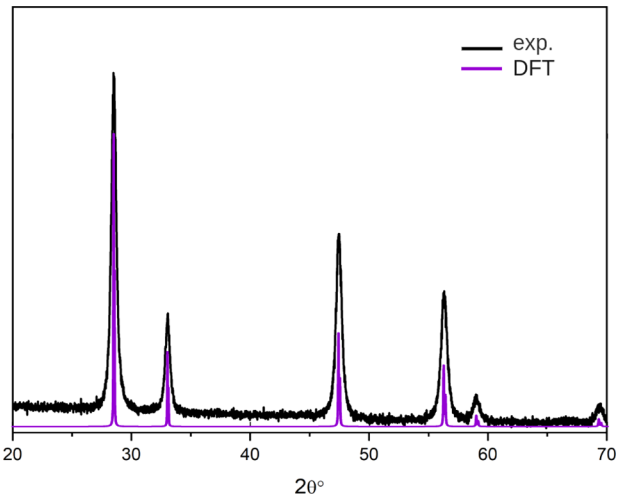

Figure 1. Experimental (black) and theoretical (violet) X-ray powder diffraction pattern of cubic $Y_2Ce_2O_7$.

The phonon dispersion (Figure 2b) along the high-symmetry path in the first BZ shows the absence of vibrational modes in the 8−13 μm range, indicating a lack of IR-active modes in the sky−window region. This result very interestingly reveals that the presence of such modes cannot be ascribed to the pure $Y_2Ce_2O_7$ fluorite polymorph.[43] They are indeed likely to be due to the coexistence of other fluorite-derived polymorph (nominally, pyrochlore and "defect fluorite")[63] domains in the experimental samples that are difficult to resolve.[64] The extremely complex structure—not easily accessible via a single theoretical model—along with the reported tendency of fluorite-related structures to oxygen diffuse[65,66] are the key to interpret the experimental rise of the mentioned IR-active modes in the sky−window region;[43] otherwise, they are not detected at the theoretical level. Thus, if on one side, $Y_2Ce_2O_7$ is experimentally demonstrated to be a valuable starting candidate for "passive cooling skins", on the other hand, we can further improve this feature upon modulating its electronic bandgap and phonon frequencies by replacing A- and B-site cations with others able to serve our final goal. An analysis based on the abundances of individual species should prompt us to work first on A-site cation replacement, with Y being slightly less abundant than Ce. Nevertheless, we initially opted to work on the B-site cation, replacing Ce with Si. Several aspects motivate this choice: Importantly, the most stable and abundant silicon oxide, SiO_2 (α-quartz), has already been shown to have high normal emittance in the sky−window region.[16] Silicon and cerium have the same oxidation state (IV) making the replacement of Ce with Si a natural choice. Second, still in terms of

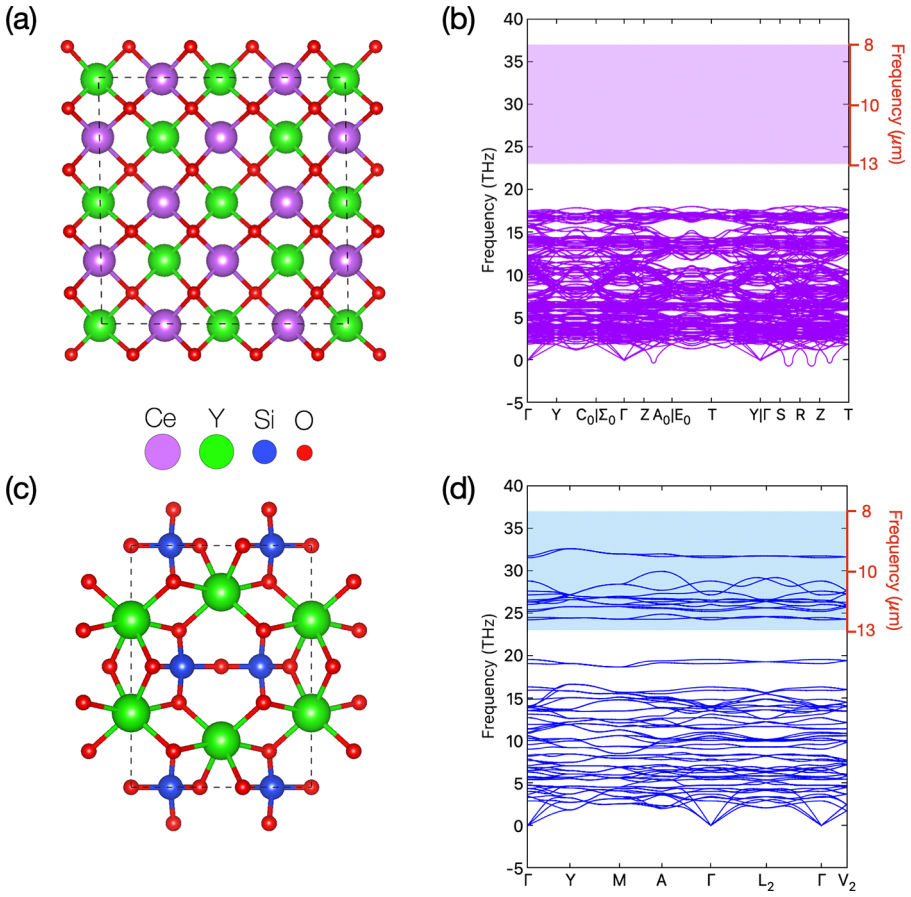

Figure 2. (a) PAW/PBE optimized structure of fluorite $Y_2Ce_2O_7$ along with its (b) phonon band structure. (The wavelength corresponding to phonon frequency is highlighted with the red right-y axis, and the sky window ranging in 8−13 μm is depicted by the shaded region with light purple color.) (c) PAW/PBE optimized structure of monoclinic, thortveitite-like, $Y_2Si_2O_7$ along with its (d) phonon band structure. (The sky window ranging in 8−13 μm is depicted by shaded region with cyan color.) [See Table 1S for the high-symmetry k-point coordinates of the Brillouin zones.]

https://doi.org/10.1021/acs.chemmater.3c01205
Chem. Mater. 2023, 35, 10384−10393

Table 1. PAW/PBE Calculated Lattice Parameters [Å], β Angle (Degrees), Energy above the Hull [eV/atoms], and Electronic Bandgap (Both PAW/PBE and HSE06, eV; *i* and *d* Refer to the *Indirect/Direct* Nature of the Bandgap) for Binary $A_2Si_2O_7$ (A = Al, Ga, In, Sc, Y, La) Parental Compounds and Equimolar Quinary $(YSGI)_2Si_2O_7$ HEO

lattice parameters	Al	Ga	In	Sc	Y	La	$Y_{0.25}Sc_{0.25}Ga_{0.25}In_{0.25}$
a	5.99	6.32	6.71	6.55	6.91	7.28	6.65
b	8.09	8.21	8.75	8.59	9.05	9.55	8.60
c	4.67	4.71	4.76	4.73	4.78	4.82	4.74
β	103.21	104.65	102.91	102.88	101.96	101.10	103.24
***E* above hull**	0.092	0.110	0.041	0.015	0.000	0.048	0.054
E_{gap}**(PBE)**	5.21 *d*	1.40 *d*	2.68 *d*	4.29 *d*	4.86 *d*	4.62 *i*	3.55 *i*
						4.66 *d*	3.58 *d*
E_{gap}**(HSE06)**	7.04 *d*	5.29 *d*	4.47 *d*	6.03 *d*	6.54 *d*	6.27 *i*	5.36 *i*
						6.31 *d*	5.37 *d*

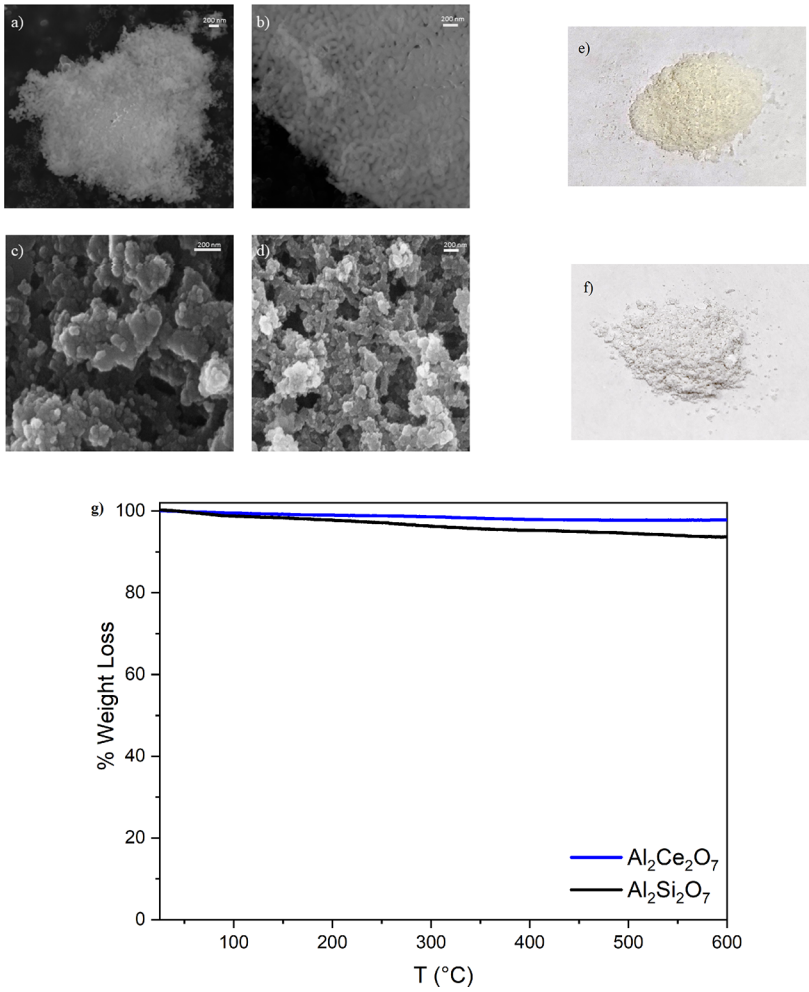

Figure 3. SEM images of (a), (b) $Al_2Ce_2O_7$ and (c), (d) $Al_2Si_2O_7$. Powders of (e) $Al_2Si_2O_7$ and (f) $Al_2Ce_2O_7$. (g) TGA curves of $Al_2Ce_2O_7$ (blue) and $Al_2Si_2O_7$ (black), respectively.

abundances, Ce is quantitatively less abundant than Si, which is not ideal for eventual scaling up and mass production. Consequently, such B-site cation replacement represents the first step for tailoring novel materials that further improve the ability of the selective IR-emitter by populating the atmospheric sky−window frequency region.[28] Structurally, moving from Ce to Si while keeping the stoichiometry of the initial compound is accompanied by a phase change from fluorite to the more stable monoclinic phase. Neither experimental synthetic procedures nor theoretical calculations were indeed able to detect the pristine fluorite structure also for $Y_2Si_2O_7$; on the other hand, as stated, among all the possible structures compatible with $Y_2Si_2O_7$ stoichiometry, our calculations reveal the monoclinic (m-) as the most stable (optimized structure reported in Figure 2c), with the stability confirmed both by the phonon band structure (reported in Figure 2d) and by the convex hull analysis reported in Table 1. It is also worth mentioning that the $Y_2Si_2O_7$ monoclinic structure (also known as β-$Y_2Si_2O_7$)—isotypic to thortveite $Sc_2Si_2O_7$[67]—is well-known from previous experimental characterizations of Becerro et al.[68,69]

https://doi.org/10.1021/acs.chemmater.3c01205
Chem. Mater. 2023, 35, 10384−10393

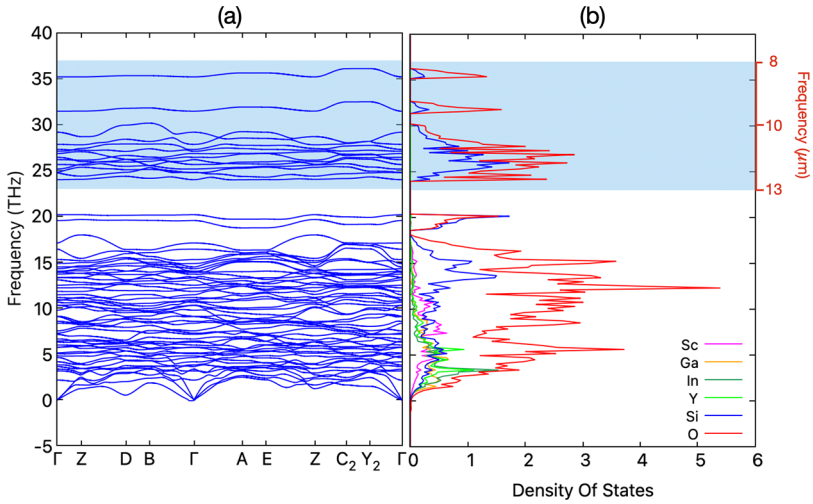

Figure 4. (a) Phonon band structure for $(Y_{0.25}Sc_{0.25}Ga_{0.25}In_{0.25})_2Si_2O_7$ HEO sampled along the high-symmetry k-point path (see Table 1S for the high-symmetry k-point coordinates) and (b) its projected density of states. [The sky window ranging in 8−13 μm is depicted by the shaded region with cyan color.]

A direct comparison in terms of phonon dispersion between m-$Y_2Si_2O_7$ and the cubic $Y_2Ce_2O_7$ in the 8−13 μm region clearly shows a marked abundance of optical modes for the former compound, thus indicating absorption of a broader wavelength range of mid-infrared (MIR) phonons in m-$Y_2Si_2O_7$. The initial B-site substitution, if on one side has the effect of reducing the symmetry of the final compound from cubic to monoclinic, on the other hand at the same time has the important consequence, fundamental for our analysis, of dragging the phonon frequencies into the long-waves region even if their distribution and density are still rather poor. Therefore, to fix such an issue, we may think of proceeding with subsequent partial substitutions on the A-site in order to achieve a better coverage of the shaded sky window region responsible for the MIR activity of such compounds. Since monoclinic $Y_2Si_2O_7$ is isotypic to thortveitite $Sc_2Si_2O_7$,[67] we can operate similar substitutions of the rare-earth A-site metal using other +3 oxidation state ions, i.e., Al, La, Sc, Ga, and In. In Table 1 we report calculated bandgaps and optimized lattice parameters for cubic $Al_2Si_2O_7$, $Ga_2Si_2O_7$, $In_2Si_2O_7$, $Sc_2Si_2O_7$, $Y_2Si_2O_7$, and $La_2Si_2O_7$, respectively, while for the same systems, Figure S1 in the Supporting Information shows phonon frequencies.

Positive combining effects can be achieved upon binary mixing on the @A-site (thereby providing a final ternary compound), as shown in Figure S2. Indeed, such operation on the @A-site (as well as the simple substitution) clearly affects the vibrational frequencies and their distribution. Anyway, the two main requirements of an efficient radiator are not met simultaneously: we obtain either wide band gap compounds (see Table S2 in the Supporting Information) or long-wave phonon frequencies homogeneously spread over the 8−13 μm range.

Therefore, it is necessary to move from m-$Y_2Si_2O_7$ to an entropy-stabilized oxide that embodies all of the features of a good MIR radiator and that can be formed when several constituting binary oxides (generally five or more) are mixed in near equimolar amounts and heated at high temperature (nonequimolar substitutions, such as ternary mixing on the @A-site, which provides a quaternary final compound, are beyond the scope of this work and will not be treated). To this aim, we exploited SQS quinary HEO random solid solution with quaternary mixing on the @A-site to ensure equimolarity (A = Ga, In, Sc, Y) using 22 atom unit cells for generating the monoclinic lattice. The relaxed lattice vectors of the final optimized structure of quinary $(YSGI)_2Si_2O_7$ SQS model HEO in its monoclinic phase are listed in Table 1.

The thermodynamic stability of an alloy is fundamental as it may influence its life cycle as well as the possibility of synthesizing the compound itself. This can be measured by the driving force for a HEO to dissociate into its most stable combination of parental compounds. In practice, this is determined by comparing the energy of the HEO with the convex energy hull of all of the constituent compounds in the relative phase diagram. Table 1 provides the energy above the hull of parental compounds and the corresponding final HEO. The ground state hulls were determined from all the calculated compounds in the Materials Project database.[60] Small energies above the hull imply that the specific material has an enhanced chance of being stabilized. When A = Al, Ga, the structures are more thermodynamically unstable (0.092 and 0.110 eV/atoms, respectively) compared to the other equivalent compounds (A = In, Sc, Y, and La), suggesting the difficulty to synthesize the former structures (A = Al, Ga). Preliminary experimental data based on our theoretical analysis show interesting results also for A = Al binary compounds: both $Al_2Ce_2O_7$ and $Al_2Si_2O_7$ have been indeed synthesized and partially characterized, as shown in Figure 3 and Figures S3−S5 (in the Supporting Information the experimental procedure is reported).

Scanning electron microscopy (SEM) measurements of $Al_2Ce_2O_7$ (Figures 3a,b) and $Al_2Si_2O_7$ (Figures 3c,d) indicate the uniformity of the particles with a semispherical shape and size of ≈30 nm. The different colors between $Al_2Ce_2O_7$ (pale yellow, Figure 3e) and $Al_2Si_2O_7$ (white, Figure 3f) are tentatively ascribed to a different structural fashion: a layered structure is likely to characterize $Al_2Ce_2O_7$.

Additionally, a straightforward structural attribution to $Al_2Si_2O_7$ is more uncertain and cumbersome (see the XRD analysis in Figure 4S in the Supporting Information). Such uncertainty is clearly due to the formation of sillimanite ($Al_2O_3{\cdot}SiO_2$) domains and of other side products that may significantly impact the final attribution. Attempts to improve

https://doi.org/10.1021/acs.chemmater.3c01205
Chem. Mater. 2023, 35, 10384−10393

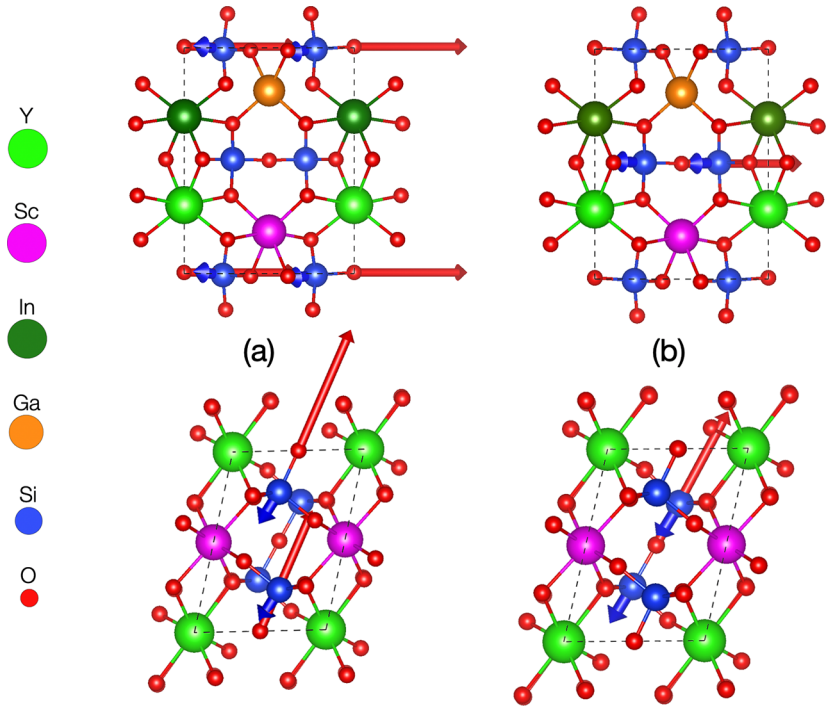

Figure 5. (a) Visualization of eigenvectors of phonon dispersion for $(Y_{0.25}Sc_{0.25}Ga_{0.25}In_{0.25})_2Si_2O_7$ HEO at **q** = 0 for ω = 35.16 THz (=8.53 μm) and (b) ω = 31.43 THz (=9.54 μm). Lateral (top) and top (bottom) orientation views for the lattice are shown.

the selectivity toward the thortveitite structure—both increasing the number of washing cycles to eliminate almost completely the residues and, alternatively, reaching higher temperatures of calcination—are nowadays in progress.

Finally, the thermogravimetric analysis (Figure 3g) shows the thermal stability of the compounds over a broad range of temperatures, up to 600 °C.

IR radiation (i.e., "thermal radiation") release is ascribed to atomic oscillations/vibrations. Experimentally, the dominant spectral range of the sky window is between 8 and 13 μm, where phonon (or vibrational) resonance peaks are essential for passive radiative cooling. At those peaks, photons are absorbed while interacting with phonons or vibrons, leading to a high absorptivity and emissivity. It is thus straightforward that the relationship between the structure of our binary compounds and their phonon spectra is the key feature for fine-tuning more complex HEOs.

The results of total DOS and partial DOS for $(YSGI)_2Si_2O_7$ are reported in Figure 4 and specifically examined to better understand the origin of the peaks in the phonon density of states (DOS). As can be seen, Figure 4 depicts two distinct frequency regions. In general, the main contribution to phonon DOS in the first region (below 20 THz) stems from oxygen vibrational modes that hybridize with metallic A-site (A = Sc, Ga, Y, In) and B-site (B = Si) ones. At higher frequencies, the A-site contribution tends to vanish, being progressively replaced by Si vibrational modes. This is particularly effective in the 23−37 THz region (corresponding to the sky−window region), where the phonon DOS clearly shows contributions from silicon and oxygen only. From the phonon spectra of the parent compounds (reported in Figure S1 in the Supporting Information), one can observe that the metal element (A-site) is responsible for the shift of the higher frequency region peaks (specific phonon modes decrease from Al (atomic mass M = 13) to In (M = 49) and further from Sc (M = 21) to La (M = 57)) while the entropy ascribed to the mixing process of the HEO formation is responsible for their splitting. Moreover, according to the space-group analysis and the eigenvectors representation of the phonon dispersion for the zone-center (**q** = 0), the frequencies at ω = 31.43 THz (=9.54 μm) and at ω = 35.16 THz (=8.53 μm) correspond to optical longitudinal vibrations with B_u irreducible representation (see Figure 5). These vibrational modes are antisymmetric by inversion and therefore IR active. It is also worth stressing that, even though (monoclinic, $C2/m$) $Ga_2Si_2O_7$ is not kinetically stable at determined ambient pressure and temperature (as shown in Figure S1 in the Supporting Information), the final HEO entails the possibility of stabilizing all the parent binary compounds into a single solid phase, as demonstrated still in Figure S1 in the Supporting Information. Indeed, this is a direct effect of the value of the configurational entropy, which becomes exceptionally large in the case of a multicomponent (generally up to 5 components) mixture, compensating for the unfavorable corresponding enthalpy contribution in the Gibbs free-energy equation.

When focusing on the electronic features of the ideal radiator, one aims to obtain materials with sufficiently wide electronic bandgaps to minimize the solar absorption in the UV−VIS region. Still, if some of the considered materials were to absorb (and consequently emit) some light for specific purposes (e.g., brightening up a room), direct-bandgap materials would be preferred since an enhanced emission is accompanied by reduced heating of the material itself. Tong et al.,[28] focusing on $BaSO_4$ as a candidate for radiative cooling, predicted ideal performances for all those materials that possess bandgaps larger than 4.13 eV, i.e., energy upper bound in the solar spectrum, and smaller than that of $BaSO_4$ (7.27 eV). In this sense, our HSE06 calculated bandgap for $(YSGI)_2Si_2O_7$ turns out to be an *almost* direct compound, where the indirect (D → Γ) bandgap is calculated to be 5.37

https://doi.org/10.1021/acs.chemmater.3c01205
Chem. Mater. 2023, 35, 10384−10393

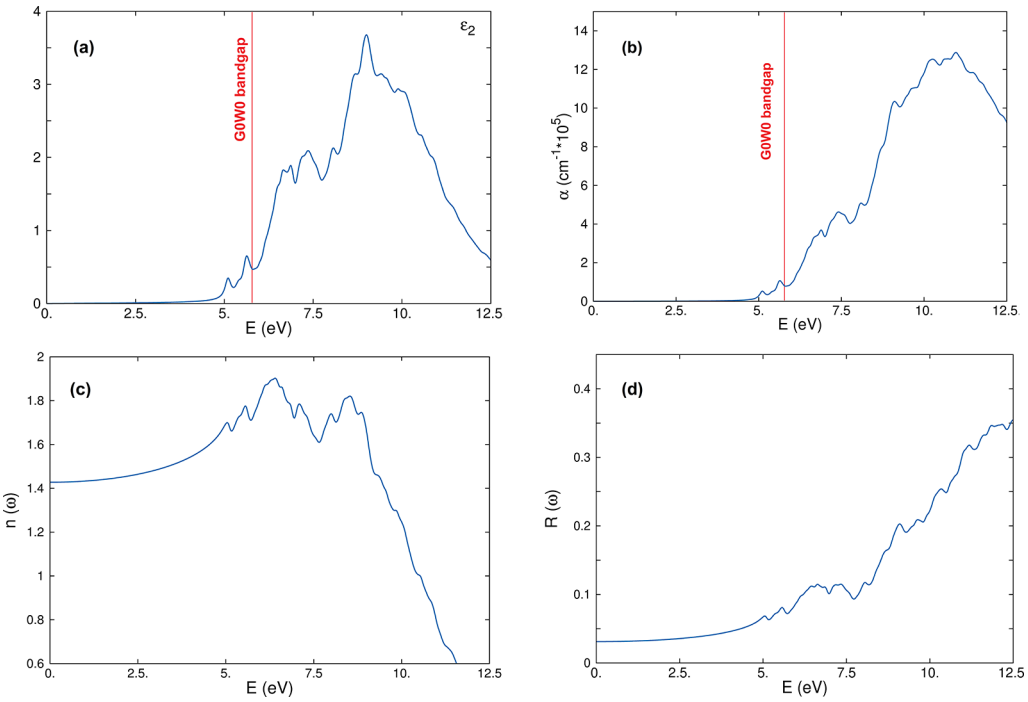

Figure 6. (a) Optical spectrum calculated at the BSE level for $(YSGI)_2Si_2O_7$. The spectrum is obtained using 20 (20) occupied (unoccupied) states in the BSE matrix. (b) Absorption spectrum still calculated at the BSE level. (c) and (d) are refractive index, $n(\omega)$, and reflectivity, $R(\omega)$, respectively, obtained at the same level of theory. The red line in (a) and (b) shows the value of the QP bandgap calculated at the G_0W_0 level of theory.

eV, only 0.01 eV smaller than the direct ($\Gamma \rightarrow \Gamma$) calculated one (5.36 eV; see Table 1). Another relevant feature to discuss is the highly desirable flatness of the bandedges of the material. Effective masses of the two carriers should be ideally infinite to maximize the recombination of any eventual excitation from the VBM to the CBM. This requirement is only partially fulfilled by our HEO since the PAW/PBE calculated electronic band structure reported in Figure S6 in the Supporting Information clearly shows a VBM almost flat with a hole effective mass that is 59.06 m_0, while the CBM shows a more dispersive behavior with an electron effective mass that is ~0.650 m_0. Nevertheless, a comparison with photocarrier effective masses calculated for α-quartz[70] and orthorhombic $BaSO_4$ at the same level of theory reveals faster carriers for these two materials (m_h = 11.5 m_0; m_e = 0.496 m_0 for SiO_2 and m_h = 2.299m_0; m_e = 0.469m_0 for $BaSO_4$, respectively) further endorsing the better performances also in this respect of $(YSGI)_2Si_2O_7$.

The optical properties (imaginary part of the dielectric function, ϵ_2, absorption, refractive index, and reflectivity) of β-$(YSGI)_2Si_2O_7$ are reported in Figure 6. A large renormalization of the DFT bandgap is obtained when calculating the QP bandgap at the "one-shot", G_0 W_0, level of theory. The so-calculated bandgap (5.78 eV) is consistent with the HSE06 calculated one. For the sake of comparison, we calculated the QP bandgap for α-quartz (SiO_2) obtaining a value of 8.76 eV, a result that well reproduces the range of the experimental values,[71,72] validating our setup (see Figures S7−S10 in the Supporting Information).

Finally, we have calculated the Born effective charge (Z^*) of the constituent ions for the β-$(YSGI)_2Si_2O_7$ structure. The static charges or the nominal charges of @A-site (A = Y, Sc, In, Ga), @B-site (B = Si) and oxygen in $(YSGI)_2Si_2O_7$ are +3, +4 and −2, respectively. From the values of Z^* tensors reported in Table S2 in the Supporting Information, in our theoretical model, constituent ions developed a maximum effective charge of 4.10 for the @A-site, 3.69 for the @B-site, and −3.37 for the @C-site, showing +37%, −8%, and +68% change from the static charge, respectively, for each ion. Furthermore, the calculated dielectric tensors (Table S3 in the Supporting Information), show a slightly anisotropic behavior with presence of off-diagonal tensor elements, coherently with the monoclinic character of the structure. In the transparent spectral range (E < 4 eV), this off-diagonal element is small (~0.04). With the knowledge of Z^* values and the dielectric constant, we can apply the so-called no analytic term correction (NAC). As shown in Figure S11 in the Supporting Information, one can see that the NAC term removes the slightly imaginary strains of the acoustic modes at Γ and shows the absence of and longitudinal optical−transverse optical (LO−TO) splitting at the Γ point, which is consistent with the nonpolar character of β-$(YSGI)_2Si_2O_7$.

■ CONCLUSIONS

Passive daytime radiative cooling is a promising phenomenon recently proposed for abating urban overheating and reducing the consequent thermal comfort deterioration in the built environment. Adequate passive coolers should reflect most of the incoming UV, VIS, and near-infrared radiation, while dissipating excess heat selectively in the specific waveband range of the atmospheric window. Designing, producing, and testing such a material is a compelling challenge for researchers worldwide that can only be addressed by tackling our current lack of knowledge about candidate materials' structural and optoelectronic features. Motivated by the impressive prospect of selective daytime radiative cooling, this work proposes high-entropy oxides as a class of potential candidates to this aim.

https://doi.org/10.1021/acs.chemmater.3c01205
Chem. Mater. 2023, 35, 10384−10393

By combining density functional theory, many-body perturbation theory, and the finite difference method, we investigate phonon band structure, electronic bandgap, optical features, and carrier effective masses aiming to predict the expected performance of the proposed compounds. More in detail, moving from the most recent experimental results in the literature, we have characterized structurally and electronically the archetypal compound $Y_2Ce_2O_7$. Results show that further substitutions in both A-site and B-site ionic positions lead to impressive changes in the phonon band structure, populating with IR-active frequency modes the region of interest (atmospheric sky−window). Overall, our finely tailored material $(Y_{0.25}Sc_{0.25}Ga_{0.25}In_{0.25})_2Si_2O_7$ satisfies the optimal electronic properties and homogeneous phonon distribution in the region of interest as requested for an efficient process. In the present work, we propose ab initio calculations as an effective tool for advanced material design and development in the field of radiative cooling. We therefore expanded the possible technological applications of high-entropy oxides, an emerging class of materials, investigating their potential for daytime passive radiative cooling applications. Finally, we explore the possible benefits of this relevant technology that could effectively mitigate detrimental urban overheating effects and reduce anthropogenic CO_2 production.

■ ASSOCIATED CONTENT

Supporting Information

The Supporting Information is available free of charge at https://pubs.acs.org/doi/10.1021/acs.chemmater.3c01205.

Experimental procedure; FTIR spectra, solar reflection and MIR emittance; phonon band structure of parental compounds (binary and ternary oxides); Brillouin zone of the investigated compounds; bare PAW/PBE bandgaps; Born effective charges; BSE calculated optical spectrum, absorption spectrum, refractive index, and reflectivity for SiO_2 (PDF)

■ AUTHOR INFORMATION

Corresponding Authors

Ivano E. Castelli − *Department of Energy Conversion and Storage, Technical University of Denmark, DK-2800 Kgs. Lyngby, Denmark;* orcid.org/0000-0001-5880-5045; Phone: +45 45258206; Email: ivca@dtu.dk

Anna Laura Pisello − *Department of Engineering, Università degli Studi di Perugia, Perugia 06125, Italy; CIRIAF − Interuniversity Research Centre, University of Perugia, Perugia 06125, Italy;* orcid.org/0000-0002-4527-6444; Phone: +39 075 5853563; Email: anna.pisello@unipg.it

Giacomo Giorgi − *Department of Civil & Environmental Engineering (DICA), University of Perugia, Perugia 06125, Italy; CIRIAF − Interuniversity Research Centre, University of Perugia, Perugia 06125, Italy; CNR-SCITEC, Perugia 06123, Italy;* orcid.org/0000-0003-4892-7908; Phone: +39 075 5853836; Email: giacomo.giorgi@unipg.it

Authors

Costanza Borghesi − *Department of Civil & Environmental Engineering (DICA), University of Perugia, Perugia 06125, Italy; CIRIAF − Interuniversity Research Centre, University of Perugia, Perugia 06125, Italy*

Claudia Fabiani − *Department of Engineering, Università degli Studi di Perugia, Perugia 06125, Italy; CIRIAF − Interuniversity Research Centre, University of Perugia, Perugia 06125, Italy*

Roberto Bondi − *Nano4Light Lab, Department of Chemistry, Biology and Biotechnology, University of Perugia, Perugia 06123, Italy*

Loredana Latterini − *Nano4Light Lab, Department of Chemistry, Biology and Biotechnology, University of Perugia, Perugia 06123, Italy;* orcid.org/0000-0002-1021-9423

Complete contact information is available at: https://pubs.acs.org/10.1021/acs.chemmater.3c01205

Notes

The authors declare no competing financial interest.

■ ACKNOWLEDGMENTS

The authors thank the ERC StG Project HELIOS (GA 101041255, PI dr. A.L. Pisello) funded by the European Commission under the framework of Horizon Europe program. Views and opinions expressed are however those of the author(s) only and do not necessarily reflect those of the European Union or the European Research Council. Neither the European Union nor the granting authority can be held responsible for them. G.G. and C.B. acknowledge ISCRA B, and C initiatives for awarding access to computing resources on m100 at CINECA SuperComputer Center, Italy and thank the Dipartimento di Ingegneria Civile e Ambientale of the University of Perugia for allocated computing time within the program "Dipartimenti di Eccellenza 2018-2022". L.L. acknowledges the Universitàà di Perugia and the Ministero per l'Università e la Ricerca Scientifica (MUR - Rome) for support through the program "Dipartimenti di Eccellenza 2018-2022" (grant AMIS). L.L. is grateful to CSGI (Consorzio Interuniversitario per lo Sviluppo dei Sistemi a Grande Interfase, Research Center for Colloid and Surface Science) for the scientific support. R.B. acknowledges MUR for the fellowship PON "Ricerca e innovazione" 2014-2020. I.E.C. acknowledges support from the Independent Research Fund Denmark (Research Project 1, "Rational Design of High-Entropy Oxides for Protonic Ceramic Fuel Cells (HERCULES)" under grant number 1032-00269B). G.G. wants to thanks Prof. Stefano Leoni of Cardiff University for the fruitful and stimulating scientific discussions.

■ REFERENCES

(1) Calm, J. M. Emissions and environmental impacts from air-conditioning and refrigeration systems. *Int. J. Refrig.* **2002**, *25*, 293−305.

(2) Meinshausen, M.; Smith, S. J.; Calvin, K.; Daniel, J. S.; Kainuma, M. L.; Lamarque, J.-F.; Matsumoto, K.; Montzka, S. A.; Raper, S. C.; Riahi, K. others The RCP greenhouse gas concentrations and their extensions from 1765 to 2300. *Climatic change* **2011**, *109*, 213−241.

(3) Fabiani, C.; Pisello, A. L.; Bou-Zeid, E.; Yang, J.; Cotana, F. Adaptive measures for mitigating urban heat islands: The potential of thermochromic materials to control roofing energy balance. *Appl. Ener.* **2019**, *247*, 155−170.

(4) Paolini, R.; Zani, A.; MeshkinKiya, M.; Castaldo, V. L.; Pisello, A. L.; Antretter, F.; Poli, T.; Cotana, F. The hygrothermal performance of residential buildings at urban and rural sites: Sensible and latent energy loads and indoor environmental conditions. *Energy and Buildings* **2017**, *152*, 792−803.

(5) Kousis, I.; Pigliautile, I.; Pisello, A. L. Intra-urban microclimate investigation in urban heat island through a novel mobile monitoring system. *Sci. Rep.* **2021**, *11*, 9732.

(6) Santamouris, M. *Minimizing energy consumption, energy poverty and global and local climate change in the built environment: innovating to zero: causalities and impacts in a zero concept world*; Elsevier, 2018.
(7) Santamouris, M.; Kolokotsa, D. On the impact of urban overheating and extreme climatic conditions on housing, energy, comfort and environmental quality of vulnerable population in Europe. *Energy Build.* **2015**, *98*, 125−133.
(8) Kojima, A.; Teshima, K.; Shirai, Y.; Miyasaka, T. Organometal halide perovskites as visible-light sensitizers for photovoltaic cells. *J. Am. Chem. Soc.* **2009**, *131*, 6050−6051.
(9) Giorgi, G.; Fujisawa, J.-I.; Segawa, H.; Yamashita, K. Small photocarrier effective masses featuring ambipolar transport in methylammonium lead iodide perovskite: a density functional analysis. *J. Phys. Chem. Lett.* **2013**, *4*, 4213−4216.
(10) Giorgi, G.; Fujisawa, J.-I.; Segawa, H.; Yamashita, K. Cation role in structural and electronic properties of 3D organic−inorganic halide perovskites: A DFT analysis. *J. Phys. Chem. C* **2014**, *118*, 12176−12183.
(11) Kawai, H.; Giorgi, G.; Marini, A.; Yamashita, K. The mechanism of slow hot-hole cooling in lead-iodide perovskite: first-principles calculation on carrier lifetime from electron−phonon interaction. *Nano Lett.* **2015**, *15*, 3103−3108.
(12) Manzhos, S.; Chueh, C.-C.; Giorgi, G.; Kubo, T.; Saianand, G.; Luder, J.; Sonar, P.; Ihara, M. Materials design and optimization for next-generation solar cell and light-emitting technologies. *J. Phys. Chem. Lett.* **2021**, *12*, 4638−4657.
(13) Carlosena, L.; Ruiz-Pardo, Á.; Feng, J.; Irulegi, O.; Hernández-Minguillón, R. J.; Santamouris, M. On the energy potential of daytime radiative cooling for urban heat island mitigation. *Sol. Energy* **2020**, *208*, 430−444.
(14) Catalanotti, S.; Cuomo, V.; Piro, G.; Ruggi, D.; Silvestrini, V.; Troise, G. The radiative cooling of selective surfaces. *Sol. Energy* **1975**, *17*, 83−89.
(15) Granqvist, C.; Hjortsberg, A. Radiative cooling to low temperatures: General considerations and application to selectively emitting SiO films. *J. Appl. Phys.* **1981**, *52*, 4205−4220.
(16) Raman, A. P.; Anoma, M. A.; Zhu, L.; Rephaeli, E.; Fan, S. Passive radiative cooling below ambient air temperature under direct sunlight. *Nature* **2014**, *515*, 540−544.
(17) Rephaeli, E.; Raman, A.; Fan, S. Ultrabroadband photonic structures to achieve high-performance daytime radiative cooling. *Nano Lett.* **2013**, *13*, 1457−1461.
(18) Hossain, M. M.; Gu, M. Radiative cooling: principles, progress, and potentials. *Adv. Sci.* **2016**, *3*, 1500360.
(19) Kou, J.-l.; Jurado, Z.; Chen, Z.; Fan, S.; Minnich, A. J. Daytime radiative cooling using near-black infrared emitters. *Acs Photonics* **2017**, *4*, 626−630.
(20) Zhao, B.; Hu, M.; Ao, X.; Chen, N.; Pei, G. Radiative cooling: A review of fundamentals, materials, applications, and prospects. *Appl. Energy* **2019**, *236*, 489−513.
(21) Li, Z.; Chen, Q.; Song, Y.; Zhu, B.; Zhu, J. Fundamentals, materials, and applications for daytime radiative cooling. *Adv. Mater. Technol.* **2020**, *5*, 1901007.
(22) Zhai, Y.; Ma, Y.; David, S. N.; Zhao, D.; Lou, R.; Tan, G.; Yang, R.; Yin, X. Scalable-manufactured randomized glass-polymer hybrid metamaterial for daytime radiative cooling. *Science* **2017**, *355*, 1062−1066.
(23) Gentle, A. R.; Smith, G. B. A subambient open roof surface under the Mid-Summer sun. *Adv. Sci.* **2015**, *2*, 1500119.
(24) Huang, Z.; Ruan, X. Nanoparticle embedded double-layer coating for daytime radiative cooling. *Int. J. Heat Mass Transfer* **2017**, *104*, 890−896.
(25) Li, X.; Peoples, J.; Huang, Z.; Zhao, Z.; Qiu, J.; Ruan, X. Full Daytime Sub-ambient Radiative Cooling in Commercial-like Paints with High Figure of Merit. *Cell Rep. Phys. Sci.* **2020**, *1*, 100221.
(26) Xu, Z.; Li, N.; Liu, D.; Huang, X.; Wang, J.; Wu, W.; Zhang, H.; Liu, H.; Zhang, Z.; Zhong, M. A new crystal $Mg_{11}(HPO_3)_8(OH)_6$ for daytime radiative cooling. *Sol. Energy Mater. Sol. Cells* **2018**, *185*, 536−541.
(27) Mandal, J.; Fu, Y.; Overvig, A. C.; Jia, M.; Sun, K.; Shi, N. N.; Zhou, H.; Xiao, X.; Yu, N.; Yang, Y. Hierarchically porous polymer coatings for highly efficient passive daytime radiative cooling. *Science* **2018**, *362*, 315−319.
(28) Tong, Z.; Peoples, J.; Li, X.; Yang, X.; Bao, H.; Ruan, X. Atomistic characteristics of ultra-efficient radiative cooling paint pigments: the case study of $BaSO_4$. *Mater. Today Phys.* **2022**, *24*, 100658.
(29) Yeh, J.-W.; Chen, S.-K.; Lin, S.-J.; Gan, J.-Y.; Chin, T.-S.; Shun, T.-T.; Tsau, C.-H.; Chang, S.-Y. Nanostructured high-entropy alloys with multiple principal elements: novel alloy design concepts and outcomes. *Adv. Engin. Mater.* **2004**, *6*, 299−303.
(30) Cantor, B.; Chang, I.; Knight, P.; Vincent, A. Microstructural development in equiatomic multicomponent alloys. *Mater. Sci. Eng., A* **2004**, *375*, 213−218.
(31) Rost, C. M.; Sachet, E.; Borman, T.; Moballegh, A.; Dickey, E. C.; Hou, D.; Jones, J. L.; Curtarolo, S.; Maria, J.-P. Entropy-stabilized oxides. *Nature commun.* **2015**, *6*, 8485.
(32) Zhang, R.-Z.; Reece, M. J. Review of high entropy ceramics: design, synthesis, structure and properties. *J. Mater. Chem. A* **2019**, *7*, 22148−22162.
(33) Bérardan, D.; Franger, S.; Dragoe, D.; Meena, A. K.; Dragoe, N. Colossal dielectric constant in high entropy oxides. *physica status solidi (RRL)−Rapid Research Letters* **2016**, *10*, 328−333.
(34) Bérardan, D.; Franger, S.; Meena, A.; Dragoe, N. Room temperature lithium superionic conductivity in high entropy oxides. *J. Mater. Chem. A* **2016**, *4*, 9536−9541.
(35) Zhao, C.; Ding, F.; Lu, Y.; Chen, L.; Hu, Y.-S. High-entropy layered oxide cathodes for sodium-ion batteries. *Angew. Chem., Int. Ed.* **2020**, *59*, 264−269.
(36) Edalati, P.; Wang, Q.; Razavi-Khosroshahi, H.; Fuji, M.; Ishihara, T.; Edalati, K. Photocatalytic hydrogen evolution on a high-entropy oxide. *J. Mater. Chem. A* **2020**, *8*, 3814−3821.
(37) Nguyen, T. X.; Liao, Y.-C.; Lin, C.-C.; Su, Y.-H.; Ting, J.-M. Advanced high entropy perovskite oxide electrocatalyst for oxygen evolution reaction. *Adv. Funct. Mater.* **2021**, *31*, 2101632.
(38) Löffler, T.; Savan, A.; Garzón-Manjón, A.; Meischein, M.; Scheu, C.; Ludwig, A.; Schuhmann, W. Toward a paradigm shift in electrocatalysis using complex solid solution nanoparticles. *ACS Energy Lett.* **2019**, *4*, 1206−1214.
(39) Sarkar, A.; Velasco, L.; Wang, D.; Wang, Q.; Talasila, G.; de Biasi, L.; Kübel, C.; Brezesinski, T.; Bhattacharya, S. S.; Hahn, H. others High entropy oxides for reversible energy storage. *Nature Commun.* **2018**, *9*, 3400.
(40) Braun, J. L.; Rost, C. M.; Lim, M.; Giri, A.; Olson, D. H.; Kotsonis, G. N.; Stan, G.; Brenner, D. W.; Maria, J.-P.; Hopkins, P. E. Charge-induced disorder controls the thermal conductivity of entropy-stabilized oxides. *Adv. Mater.* **2018**, *30*, 1805004.
(41) Zhang, H. S.; Liao, S. R.; Yuan, W.; Guan, S. K. Preparation and thermal conductivity of Y_2 Ce_2 O_7 ceramic material. *Adv. Mater. Res.* **2011**, *266*, 59−62.
(42) Du, T.; Niu, J.; Wang, L.; Bai, J.; Wang, S.; Li, S.; Fan, Y. Daytime Radiative Cooling Coating Based on the Y_2O_3/TiO_2 Microparticle-Embedded PDMS Polymer on Energy-Saving Buildings. *ACS Appl. Mater. Interface* **2022**, *14*, 51351−51360.
(43) Dang, S.; Xiang, J.; Yao, H.; Yang, F.; Ye, H. Color-preserving daytime passive radiative cooling based on Fe3+-doped Y_2 Ce_2 O_7. *Energy Build.* **2022**, *259*, 111861.
(44) Kresse, G.; Hafner, J. Ab initio molecular dynamics for open−shell transition metals. *Phys. Rev. B* **1993**, *48*, 13115−13118.
(45) Kresse, G.; Hafner, J. Ab initio molecular−dynamics simulation of the liquid−metal−amorphous−semiconductor transition in germanium. *Phys. Rev. B* **1994**, *49*, 14251−14269.
(46) Kresse, G.; Furthmüller, J. Efficiency of ab−initio total energy calculations for metals and semiconductors using a plane−wave basis set. *Comput. Mater. Sci.* **1996**, *6*, 15−50.
(47) Kresse, G.; Furthmüller, J. Efficient iterative schemes for ab initio total−energy calculations using a plane−wave basis set. *Phys. Rev. B* **1996**, *54*, 11169−11186.

(48) Perdew, J. P.; Burke, K.; Ernzerhof, M. Generalized Gradient Approximation Made Simple. *Phys. Rev. Lett.* **1996**, *77*, 3865−3868.
(49) Blöchl, P. E. Projector augmented-wave method. *Phys. Rev. B* **1994**, *50*, 17953.
(50) Kresse, G.; Joubert, D. From ultrasoft pseudopotentials to the projector augmented-wave method. *Phys. Rev. B* **1999**, *59*, 1758.
(51) Togo, A.; Tanaka, I. First principles phonon calculations in materials science. *Scripta Mater.* **2015**, *108*, 1−5.
(52) Krukau, A. V.; Vydrov, O. A.; Izmaylov, A. F.; Scuseria, G. E. Influence of the exchange screening parameter on the performance of screened hybrid functionals. *J. Chem. Phys.* **2006**, *125*, 224106.
(53) Onida, G.; Reining, L.; Rubio, A. Electronic excitations: density-functional versus many-body Green's-function approaches. *Rev. Mod. Phys.* **2002**, *74*, 601.
(54) Dancoff, S. Non-adiabatic meson theory of nuclear forces. *Phys. Rev.* **1950**, *78*, 382.
(55) Zunger, A.; Wei, S.-H.; Ferreira, L.; Bernard, J. E. Special quasirandom structures. *Phys. Rev. Lett.* **1990**, *65*, 353.
(56) Van de Walle, A.; Tiwary, P.; De Jong, M.; Olmsted, D.; Asta, M.; Dick, A.; Shin, D.; Wang, Y.; Chen, L.-Q.; Liu, Z.-K. Efficient stochastic generation of special quasirandom structures. *CALPHAD* **2013**, *42*, 13−18.
(57) Van De Walle, A.; Asta, M.; Ceder, G. The alloy theoretic automated toolkit: A user guide. *CALPHAD* **2002**, *26*, 539−553.
(58) van de Walle, A.; Ceder, G. Automating first-principles phase diagram calculations. *J. Phase Equilib.* **2002**, *23*, 348−359.
(59) Van De Walle, A. Multicomponent multisublattice alloys, nonconfigurational entropy and other additions to the Alloy Theoretic Automated Toolkit. *CALPHAD* **2009**, *33*, 266−278.
(60) Jain, A.; Ong, S. P.; Hautier, G.; Chen, W.; Richards, W. D.; Dacek, S.; Cholia, S.; Gunter, D.; Skinner, D.; Ceder, G. others Commentary: The Materials Project: A materials genome approach to accelerating materials innovation. *APL Mater.* **2013**, *1*, No. 011002.
(61) Raj, A. K.; Rao, P. P.; Sameera, S.; Divya, S. Pigments based on terbium-doped yttrium cerate with high NIR reflectance for cool roof and surface coating applications. *Dyes Pigm.* **2015**, *122*, 116−125.
(62) Nishino, H.; Yamamura, H.; Arai, T.; Kakinuma, K.; Nomura, K. Effect of cation radius ratio and unit cell free volume on oxide-ion conductivity in oxide systems with pyrochlore-type composition. *J. Ceram. Soc. Jpn.* **2004**, *112*, 541−546.
(63) Liu, Y.; Withers, R. L.; Norén, L. The pyrochlore to 'defect fluorite'transition in the Y_2 $(Zr_y$ $Ti_{1-y})_2$ O_7 system and its underlying crystal chemistry. *J. Solid State Chem.* **2004**, *177*, 4404−4412.
(64) Van Dijk, M.; Mijlhoff, F.; Burggraaf, A. Pyrochlore microdomain formation in fluorite oxides. *J. Solid State Chem.* **1986**, *62*, 377−385.
(65) Van Dijk, M.; De Vries, K.; Burggraaf, A. Oxygen ion and mixed conductivity in compounds with the fluorite and pyrochlore structure. *Solid State Ionics* **1983**, *9*, 913−919.
(66) Ikuma, Y.; Tsubaki, Y.; Nakao, Y.; Yokogawa, Y.; Yoshimura, M. Oxygen diffusion in the fluorite-related phases of Y_2 O_3 -Ta_2 O_5 and Ho_2 O_3 -Ta_2 O_5 systems. *Solid state ionics* **1990**, *40*, 258−261.
(67) Redhammer, G. u. J.; Roth, G. β-Y2Si2O7, a new thortveitite-type compound, determined at 100 and 280 K. *Acta Crystallogr.Sect.C* **2003**, *59*, i103−i106.
(68) Becerro, A. I.; Escudero, A.; Florian, P.; Massiot, D.; Alba, M. D. Revisiting $Y_2Si_2O_7$ and Y_2SiO_5 polymorphic structures by 89Y MAS-NMR spectroscopy. *J. Solid State Chem.* **2004**, *177*, 2783−2789.
(69) Becerro, A. I.; Escudero, A. XRD and ^{29}Si MAS-NMR spectroscopy across the β-$Lu_2Si_2O_7$−β -$Y_2Si_2O_7$ solid solution. *J. Solid State Chem.* **2005**, *178*, 1−7.
(70) Glinnemann, J.; King, H., Jr; Schulz, H.; Hahn, T.; La Placa, S.; Dacol, F. Crystal structures of the low-temperature quartz-type phases of SiO_2 and GeO_2 at elevated pressure. *Z. fur Krist. - Cryst. Mater.* **1992**, *198*, 177−212.
(71) Evrard, R.; Trukhin, A. Photoelectric properties and the energy gap of SiO_2. *Phys. Rev. B* **1982**, *25*, 4102.
(72) Trukhin, A. Investigation of the photoelectric and photo-luminescent properties of crystalline quartz and vitreous silica in the fundamental absorption region. A model for electronic structure and migration of energy in SiO_2. *Phys. Status Solidi B* **1978**, *86*, 67−75.

https://doi.org/10.1021/acs.chemmater.3c01205
Chem. Mater. 2023, 35, 10384−10393